

Radiolabeled Human Protein-Functionalized Upconversion Nanoparticles for Multimodal Cancer Imaging

Najim Akhtar, Pei-Wen Wu, Chuan Lin Chen, Wen-Yi Chang, Ren-Shyan Liu, Chien Ting Wu, Agnishwar Girigoswami, and Surojit Chattopadhyay*



Cite This: *ACS Appl. Nano Mater.* 2022, 5, 7051–7062



Read Online

ACCESS |



Metrics & More



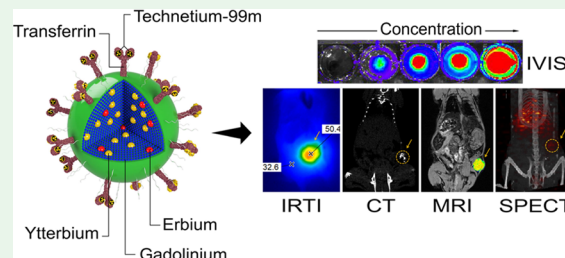
Article Recommendations



Supporting Information

ABSTRACT: Multimodal imaging removes the intrinsic limitations of individual modalities, while the multipurpose nanoagents reduce the toxicity associated with the use of multiple contrast agents. However, limited functionality, inefficient or incompatible targeting, and unknown biodistribution are significant drawbacks for such complicated nanode-signs. We report a biofriendly pentamodal imaging agent with the synergistic dual-targeting ability (passive and active) based on fluoromagnetic NaGdF₄:Yb,Er upconverting nanoparticles (UCNPs). Besides the nano-enabled passive targeting, the apo-human serum transferrin protein (Tf) conjugation actively targets the transferrin receptors (TfR) over-expressed on different cancer cells. The radiolabel, ^{99m}Tc, chelates in the Tf core increase the radiolabeling efficiency (~95%) and stability (~100% for 24 h), enabling efficient single-photon emission computed tomography imaging. Deep-penetrating 980 nm excited UCNPs are inherently active luminescent and photothermal agents enabling fluorescence and photothermal imaging, respectively. The Gd in UCNPs produces a T1-weighted MRI signal, and the Yb helps in computed tomography (CT) as contrast agents. A pentamodal imaging agent (UCNP@Tf-^{99m}Tc) with synergistic dual-targeting ability is thus designed. In vitro studies demonstrated receptor-mediated endocytosis and minimal cytotoxicity of the UCNPs. The in vivo biodistribution studies in the mice model under SPECT/CT revealed its near-ideal bioavailability and renal clearance behavior. The MRI investigation on 4 T1 tumor-bearing mice brought direct evidence of passive and synergistic passive-active targeted tumor accumulation of the nanoformulation. The in vivo multimodal tumor imaging (MRI/SPECT/thermal-camera/CT) demonstrates the potency of UCNPs@Tf-^{99m}Tc as a single replacement for multiple imaging agents and a perfect candidate for the ultramodern Advanced Multimodality Image Guided Operating (AMIGO) suite.

KEYWORDS: upconversion nanoparticles, cancer targeting, transferrin, multimodal imaging, ^{99m}Tc



INTRODUCTION

Research-level bioimaging aims to extend capabilities beyond tumors, probing the subcellular or molecular microenvironment.^{1–3} Varied modalities, namely, magnetic resonance imaging (MRI),⁴ computed tomography (CT),⁵ single-photon emission computed tomography (SPECT),² fluorescence-based imaging,^{6,7} and many more are thus accessed regularly in clinical and laboratory settings. However, heterogeneity of different tumors and physiological differences in clinical subjects rendered these individual imaging modalities insufficient to provide the necessary accuracy and reliable details.³ For example, CT, a high-resolution tissue characterizing technique that can give volumetric images of the human organ, is limited by the requirement of relatively high radiation doses compared to projection radiography.⁸ On the other hand, MRI is insensitive to molecular- and cellular-level details until recently.⁹ SPECT can provide excellent sensitivity, but the uncontrolled distribution of the radioisotope,¹⁰ lack of soft-tissue contrast, and low resolution are its limitations.¹⁰

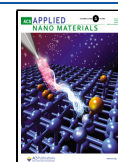
Fluorescence-based imaging offers multiscale, single cell to whole body, imaging, yet limited by the poor penetration of the short wavelength excitation of the imaging agents.¹¹

To alleviate the limitations in each of these individual imaging modalities, single nanoparticle systems were designed to impart multimodal imaging functionalities that complement each other.^{12,13} This offers additional benefits, such as (i) a single dose of the agent for comprehensive diagnosis and limiting associated toxicity from multiple dosages; (ii) saving time as multiple dosages of agents cannot be administered in quick succession. These advantages motivate researchers to develop a range of nano-enabled multimodal imaging agents,

Received: March 8, 2022

Accepted: April 27, 2022

Published: May 11, 2022



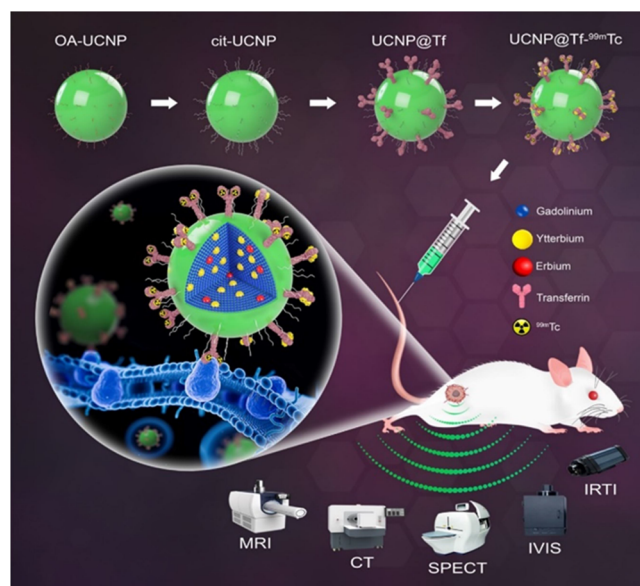
for example, quantum dots,¹⁴ gold nanorods,¹⁵ AION (silver sulfide and iron oxide nanoparticles in PEGylated micelles),¹⁶ silica–iron oxide nanoparticles (SIO NPs),¹⁷ copper sulfide nanoparticles (CuS NPs),¹⁸ and so on. The general challenges facing the clinical application of these NPs are their biocompatibility, safe renal clearance, and active targeting capability. Other technical limitations do exist. For example, quantum dots are excited in the ultraviolet and visible (UV–vis)¹⁴ regions and are unsuitable for deep tissue imaging. Some fluorescent agents may photobleach.¹⁹ On the other hand, AION micelles,¹⁶ a composite of multiple imaging agents, lack demonstrated cancer targeting. Gold nanorods¹⁵ provide good CT and photothermal contrast but fail in other modalities. In fact, a look at Table 2 in ref 12 will reveal that most NPs show dual modality, and some of these are actively targeted with biocompatible peptides. Safe clearance of most of these NPs is rarely reported.

Ultrastable upconversion NPs (UCNPs), showing insignificant photobleaching, are excited in the low energy near-infrared window II (NIR-II), with emission in the high energy visible spectrum, and are better suited for deep tissue imaging via upconversion luminescence (UCL) imaging using a confocal microscope for *in vitro* studies²⁰ and an *in vivo* imaging system (IVIS) for small animal studies.⁷ The nonradiative recombination in the UCNPs has also demonstrated photothermal effects in the UCNPs.²¹ The photothermal heat can be easily recorded using an IR thermal imaging (IRTI) camera.²¹ The rare-earth ions such as gadolinium (Gd³⁺) and ytterbium (Yb³⁺) in these make them active under MRI²² and CT^{23,24} modalities, respectively. Besides, the facile surface functionalization, such as with –COOH²⁰ and –NH₂,²⁵ provides routes for bioconjugation. Subsequently, the possible incorporation of radioisotopes opens up the potential for SPECT or PET (positron emission tomography) imaging. Multimodal imaging using these UCNPs has also been reported,^{22–24,26} but lacking one or more attributes among (i) penta-modal capability, (ii) active targeting capability, (iii) pharmacokinetics information, (iv) biocompatibility, and (v) high required dosage for reasonable machine contrast.

As-grown UCNPs, dispersed in cyclohexane, require further surface functionalization for water dispersion, bioconjugation, and biocompatibility. To achieve this goal, different molecules have been reported, such as polyethylene glycol (PEG)²⁶ and silica coating.²⁷ However, these may still elicit an immune response.²⁸ UCNPs are generally popular for deep tissue UCL imaging utilizing the 980 nm excitation, and other modalities are scarce.^{7,20} UCNPs have also been used with well-known targeting ligands, such as RGD tripeptide for MG 87,²⁹ specific to cancer types. Many human cancer cells overexpress transferrin protein receptor (TfR), a glycoprotein that binds and internalizes transferrin protein (Tf) which carries two molecules of the iron (Fe⁴⁺)³⁰ and transports oxygen and other indispensable micronutrients to the cell, and plays a significant role in DNA synthesis.³⁰ It has been reported that the Tf–TfR interaction can be utilized to increase the uptake of drugs³¹ in cancer cells, as well as being used for actively targeted tumor imaging.³² Conjugation of an iron-free Tf (apo-transferrin) with the UCNP allows biocompatibility, and, most importantly, opens the door for chelation of metal-based radioisotopes such as In³⁺, and Tc⁴⁺ for SPECT^{32,33} and takes it to the next level as an active targeting agent.

In this study, we report the development of a biocompatible pentamodal cancer imaging agent with passive and active targeting ability using magnetic upconversion nanoparticles (UCNPs; NaGdF₄:Yb,Er), conjugated with Tf and ^{99m}Tc (Technetium-99 m) chelation into the iron cage of Tf (Scheme 1). To the best of our knowledge, this has never

Scheme 1. Schematic Illustration of the Key Nanoformulation Steps for UCNP@Tf-^{99m}Tc synthesis and Multimodal Imaging of Cancer



been demonstrated earlier. The pentamodal imaging ability of the nanoformulation was evaluated *in vitro* under IRTI, IVIS, MRI, CT, and SPECT. The cancer-targeting ability was examined under MRI. Finally, multimodal cancer imaging was performed *in vivo* in 4 T1 tumor-bearing mice under MRI, SPECT/CT, IRTI, and CT to reveal the efficacy of the UCNP@Tf-^{99m}Tc as an ideal cancer imaging agent.

MATERIALS AND METHODS

Materials. GdCl₃ (99.99%), YbCl₃ (99.99%), ErCl₃ (99.99%), and 1-(3-dimethylaminopropyl)-3-ethylcarbodiimide (EDC) were purchased from Alfa Aesar, USA. OA was purchased from Fisher Chemical, USA. Octadecene (ODE) was purchased from Sigma-Aldrich, USA. Methanol, NH₄F, and trisodium citrate were purchased from Acros Organics, USA. NaOH, apo-transferrin human (Tf), and SnCl₂ were purchased from Sigma-Aldrich, USA. Diethylene glycol (DEG) was purchased from VETEC, USA. HCl (0.1 M) was purchased from Avantor Performance Materials, USA. Ethanol was purchased from Echo Chemical, Taiwan. The ultrafiltration vials (100 kDa and 10 kDa) were purchased from Mark Millipore, Ireland. All the cell culture materials were purchased from HiMedia Laboratories, India.

Synthesis of OA-UCNPs. OA-UCNPs were synthesized by following the protocol followed in our prior study³⁴ with slight modifications. Typically, a three-neck round-bottom flask (100 mL) was taken in which 0.02 mM ErCl₃, 0.18 mM YbCl₃, and 0.8 mM GdCl₃ were mixed with 16 mL of ODE and 14 mL of OA. The solution was then heated to 150 °C under nitrogen flow for 15 min, which resulted in the formation of a homogeneous solution. The solution was cooled to 50 °C, and 10 mL of methanol solution containing 4 mM NH₄F and 2.5 mM NaOH were slowly injected under stirring (380 rpm) for 30 min at 50 °C. Subsequently, methanol from the reaction solution was evaporated by heating the reaction

system at 100 °C for 10 min. The remaining mixture was heated to 300 °C for 60 min under atmospheric pressure and nitrogen flow and cooled to room temperature. The as-synthesized magnetic OA-UCNPs (NaGdF₄:Yb,Er) were precipitated by ethanol and collected by centrifugation at 8000 for 10 min and washed with ethanol 3–4 times and finally dried under vacuum.

Citrate Functionalization. Surface modifications of the OA-UCNPs were done following a previously reported work.³⁵ In short, 100 mg of OA-UCNPs was dispersed in 60 mL of DEG in a three-neck round-bottom flask. Thereafter, 200 mg of trisodium citrate was added and heated at 200 °C under continuous stirring (280 rpm) for 3 h to ensure the ligand exchange. Once cooled to room temperature (RT), 20 mL of HCl (0.1 M) was added to precipitate the citrate-functionalized UCNPs (cit-UCNP). After an overnight precipitation, cit-UCNPs were collected by centrifugation at 15,000 rpm for 30 min, washed 2–3 times with ethanol, and redispersed in 15 mL of deionized (DI) water and then freeze-dried to obtain a pure cit-UCNP powder.

Transferrin (Tf) Conjugation. An abundant NH₂ functional group in Tf protein was utilized for the conjugation, through amide bonding, with the –COOH groups on the surface of the cit-UCNPs. In brief, 25 mL of cit-UCNP solution at a concentration of 0.2 mg/mL (in water) was taken in a glass beaker to which 5 mg of EDC was added and stirred for 2 h at 340 rpm to activate the –COOH group of the cit-UCNPs. Next, 15 mg of Tf was added and stirred for another 2 h (at 200 rpm). Upon completion of the reaction, the reactant solution was centrifuged (15,000 rpm for 30 min) to collect the Tf-conjugated UCNPs (UCNP@Tf), followed by 2–3 times of washing and freeze-drying to obtain a UCNPs@Tf powder for further use.

To evaluate the Tf loading efficiency, 0.2 mg of UCNPs was mixed with 0.6 mg of Tf and left for conjugation (24 h). Later, the solution (in PBS) was centrifuged (at 15,000 rpm) to separate the UCNPs in the precipitate and free Tf in the supernatant. The optical absorption strength of “Total Tf” (the whole solution containing UCNPs@Tf) and “Free Tf” (the obtained supernatant) at 280 nm was measured using a standard ELISA (enzyme-linked immunosorbent assay) plate reader (Infinite 200 PRO, Tecan Trading AG, Switzerland). The absorption values of “Total Tf” and “Free Tf” were then utilized to calculate the loading efficiency using the conventional loading efficiency formula [(Loading efficiency (%)) = (Total Tf – Free Tf / Total Tf) × 100%].³⁶

^{99m}Tc Labeling. The chelation of ^{99m}Tc in UCNPs@Tf was achieved by following an earlier study³² with slight modifications. Briefly, 125 μL of ^{99m}Tc-pertechnetate in DI water (50 mCi/mL) was added into 500 μL of UCNPs@Tf solution (1 mg/mL in DI water) at pH 7.0. Subsequently, 5 μL of SnCl₂ (1 mg/mL) was added to the above solution and allowed to react for 30 min at room temperature under gentle agitation. After the reaction was completed, the radiolabeling efficiency of ^{99m}Tc-labeled UCNPs@Tf (UCNPs@Tf-^{99m}Tc) was evaluated by standard Radio-TLC, using water as the mobile phase. The radioactivity at different areas of the TLC paper was examined using a radio-TLC scanner (AR-2000 radio-TLC Imaging Scanner, Bayer Healthcare Co. Ltd., China). Byproducts of the radiochemical reaction and free ^{99m}Tc, if any, were separated by an ultrafiltration tube (cutoff = 10 kDa), and the precipitate was redispersed in 0.5 mL of DI water.

Stability of UCNPs@Tf-^{99m}Tc. The stability of UCNPs@Tf-^{99m}Tc was examined using a radio-TLC scanner mentioned earlier. The TLC measurements were done under three different conditions, in phosphate buffered saline (PBS) at 4 and 37 °C, as well as in 20% fetal bovine serum (FBS) at 37 °C. As-prepared UCNPs@Tf-^{99m}Tc solution (100 μL) was mixed with 1 mL of PBS and 0.5 mL of FBS separately. Samples were stored at 37 and 4 °C and measured for their radioactivity at different time intervals using TLC.

Materials Characterization. The morphology and crystalline structures of the UCNPs were examined using transmission electron microscopy (TEM) (Philips JEM-2000EX, Country) operating at 200 kV. The optical absorption spectra of the materials were recorded by UV–vis–NIR spectrophotometer (JASCO V-770, JASCO Corp., Japan) in the range of 200–1100 nm. The UCL spectra were

recorded by fluorescence spectroscopy (Fluorolog-3, Jobin Yvon, USA) in the range of 300–1000 nm using 980 nm laser head (SDL-980-LM-5000 T, Shanghai, Dream Laser Technology, China), with a 60° angle of incident and power up to 5 W, as the excitation source. The zeta potential, PdI, and hydrodynamic diameter of different nanocomposites were measured using the particle size analyzer (Zetasizer Nano ZS, Malvern Panalytical, USA) at pH 7.0. For further confirmation of the citrate functionalization and Tf conjugation on the cit-UCNP, Fourier transform infrared (FT-IR) spectra were recorded using a FT-IR spectroscope (Spectrum GX FTIR, Perkin Elmer, USA).

Cytotoxicity Assays. To study the cell cytotoxicity, 4 T1 breast cancer cells were cultured in a 96-well plate. In each well, 0.2 mL of RPMI1640 medium containing 5000 cells was taken and incubated for 24 h at 37 °C with 5% CO₂. After 24 h of incubation, the cell culture medium was replaced with a fresh medium containing different concentrations (0 to 2 × 10³ ppm) of UCNPs@Tf and UCNPs@Tf-^{99m}Tc and incubated for another 24 h at the same condition. Next, MTT (3-(4,5-dimethylthiazol-2-yl)-2,5-diphenyltetrazolium bromide) at a concentration of 5 mg/mL was added to all the wells and further incubated for 4 h in the dark. Then, DMSO (dimethyl sulfoxide) was added to dissolve the crystals, and the absorbance at 570 nm was measured using a standard ELISA (enzyme-linked immunosorbent assay) plate reader (Infinite 200 PRO, Tecan Trading AG, Switzerland).

Cellular Uptake and Intracellular Distribution. Cellular internalization of UCNPs@Tf-^{99m}Tc was examined using confocal microscopy. 1 × 10⁵ 4 T1 cells/well were cultured on glass coverslips placed inside the wells and incubated under standard conditions. After 24 h, the cells were treated with 500 ppm of UCNPs@Tf-^{99m}Tc, and incubated for a further 24 h. Subsequently, the cells were washed thrice with PBS to remove any extracellular NPs and stained with 4,6-diamidino-2-phenylindole (DAPI) to visualize the nucleus of the cell, and 4% paraformaldehyde was introduced as the cross-linking fixation agent. Next, the coverslips with the fixed cells were carefully removed from the wells to study under a confocal laser scanning microscopy (CLSM) (Leica TCS-SP5-AOBS-MP, Germany) equipped with femtosecond Ti:sapphire laser (Chameleon Ultra 2, Coherent Inc., USA). To obtain the signals from DAPI, excitation and emission wavelengths were 405 and 461 nm, respectively. To detect the UCL of UCNPs@Tf, cells were irradiated with 980 nm, and the emission filter was set to 500–600 nm. The confocal fluorescence image processing and analysis were done with the open-source software ImageJ (developed at the National Institutes of Health and Laboratory for Optical and Computational Instrumentation, USA).

In Vitro Penta-Modal Imaging (IRTI, UCL, MRI, SPECT, and CT). The phantom imaging of the as-formulated UCNPs@Tf-^{99m}Tc was done under five different modalities: IRTI, IVIS, MRI, SPECT, and CT. First, an in vitro phantom was prepared using a 36-well cell culture plate with 0, 100, 200, 400, and 800 ppm of UCNPs@Tf-^{99m}Tc in different wells. For photothermal imaging, the phantom was placed under an IR thermal camera (P384 SERIES, Ching Hsing Computer-Tech Ltd., Taipei, Taiwan), followed by 980 nm laser (Changchun New Industries Optoelectronics Co. Ltd., China) irradiation for 7.5 min, delivered through an optical fiber with a 20 mm collimator, to obtain the photothermal images, and the temporal rise of the temperature profile. The laser (0.32 W/cm²) was irradiated at normal incidence (to the wells), and the images were captured at 45° angle to avoid any interference from reflected/unabsorbed 980 nm light. Next, the phantom was placed inside the sample chamber of the IVIS (IVIS 50, Perkin-Elmer, Massachusetts, USA) equipped with the same external 980 nm laser (0.32 W/cm²) for UCL imaging. The major emission of the UCNPs@Tf-^{99m}Tc at 545 nm was captured in the GFP (green fluorescent protein) window. All the UCL images were normalized to photon per second per cm² per steradian (p/s/cm²/sr) after removing the background signals, and the emission from different wells containing different concentrations of UCNPs@Tf-^{99m}Tc were quantified by selecting the ROI (region of interest) using Living Image software (PerkinElmer, Massachusetts, USA).

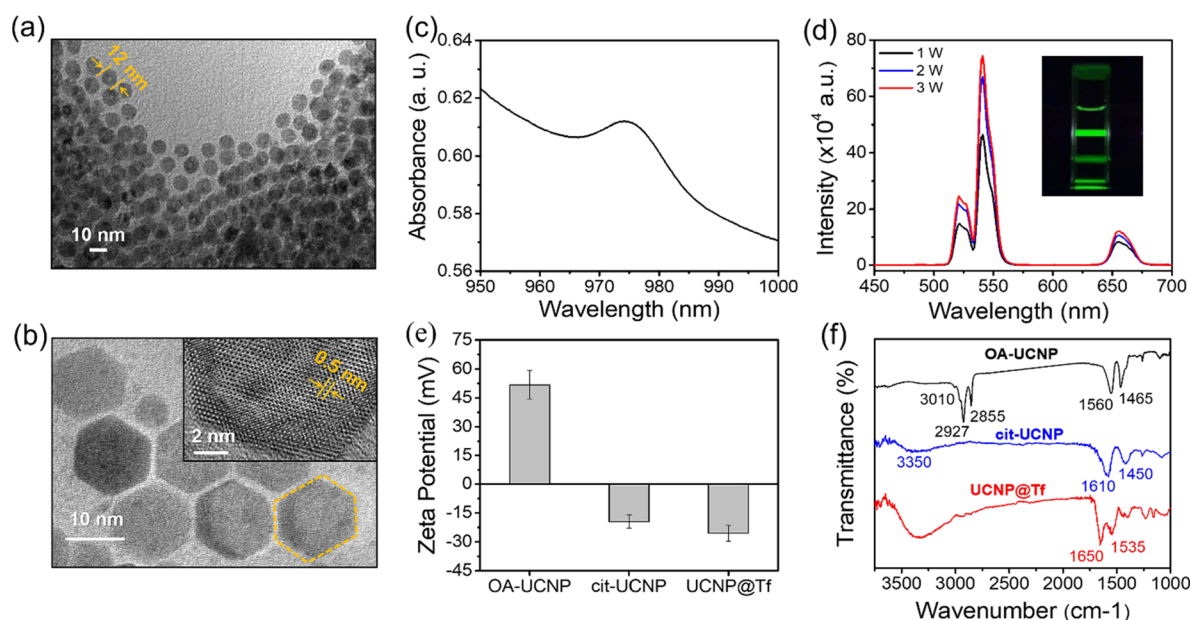


Figure 1. (a) TEM and (b) HR-TEM image demonstrating the morphology of the core NaGdF₄:Yb,Er UCNPs (OA-UCNP). The inset in (b) shows the lattice resolved HR-TEM image demonstrating the lattice spacing of the OA-UCNP nanocrystals. (c) Optical absorption spectrum of OA-UCNPs (2 mg/mL in cyclohexane) showing ~980 nm absorption band. (d) Power-dependent UCL spectra of the OA-UCNP under 980 nm laser excitation. The inset shows the optical photograph of a cuvette containing a colloidal solution of OA-UCNP, fluorescing bright green under 980 nm laser irradiation. (e) Zeta potential of OA-UCNP, cit-UCNP, and UCNPs@Tf. (f) FT-IR spectra of OA-UCNP, cit-UCNP, and UCNPs@Tf. Main absorption bands are labeled.

The in vitro T1-weighted MRI of the phantom was recorded using a 1.5 T clinical MR scanner (Signa HDxt 1.5 T, GE Healthcare, USA) using conditions published before.⁶ Briefly, repetition time (TR) = 3000 ms, echo time (TE) = 14 ms, field of view (FOV) = 24 × 24, slice thickness of 2 mm, and variable TI = 400–2000 ms were fixed for T1-weighted FLAIR. After the MR imaging, the phantom was imaged under SPECT using the Small Animal SPECT/CT system (NanoSPECT/CT, Mediso Ltd., Hungary). The images were acquired within an energy range of 150–190 keV. The number of projections was 64 (25 s/projection).

Next, a microCT system (u-CT, MILabs, Netherlands) was utilized to record the CT images of the phantom. Standard scanning parameters used were voltage = 50 kVp, slice thickness = 0.36 mm, field of view = 92.16 mm, and gantry rotation time = 1 min. The Hounsfield Units (HU) of different wells from the CT image were calculated using the formula: $HU = ((\mu_{\text{sample}} - \mu_{\text{water}})/(\mu_{\text{water}} - \mu_{\text{air}})) \times 1000$, where μ is the linear attenuation coefficient. All the raw data from MRI, CT, and SPECT were reconstructed and analyzed using open-source software AMIDE (developed at the Department of Radiology and the Bio-X Program, Stanford University, USA). The intensity values of different wells under MRI, CT, and SPECT were measured by selecting the ROI via the AMIDE software.

Animal Handling and Tumor Induction. The experimental protocols for animal handling and tumor induction were performed based on a previously published work³⁷ and approved by the Institutional Animal Care and Use Committee (IACUC) of National Yang-Ming Chiao-Tung University with IACUC approval no. 1090420 prior to the experiments. In this study, eight female mice (BALB/C; 6–8 weeks old), weighing between 20 and 30 g were purchased from the National Applied Research Laboratories, Taipei, Taiwan. The mice were housed and taken care of in the Laboratory Animal Center of National Yang-Ming Chiao-Tung University under controlled conditions (light:dark = 10:14 h) and temperature. Standard food for the mice was purchased from LabDiet, New Taipei City, Taiwan. The mice were provided with only deionized water on a schedule. Five of these mice were then subcutaneously injected with 4 T1 cell suspension (100 μ L of PBS containing 5×10^5 cells) on the dorsal side of each mouse. The tumors were left to grow for ~two

weeks from the day of tumor induction, until it reached a volume between 200 and 250 mm³, measured externally.

Biodistribution Study of UCNPs@Tf-^{99m}Tc under SPECT/CT.

To noninvasively study the biodistribution and pharmacokinetics of UCNPs@Tf-^{99m}Tc, healthy female mice (BALB/C, 6–8 weeks old) were first scanned under the small animal SPECT/CT system. The mice were then injected with 200 μ L of UCNPs@Tf-^{99m}Tc (1000 ppm, 180 μ Ci) via the tail vein and imaged at 0 (immediately after injection), 1, 2, 3, 4, 5, and 6 h postinjection. Images were acquired using an energy range of 150–190 keV. The number of projection angle was 64, time per projection was 25 s, and the field of view was 24.82 mm. The raw images were reconstructed and analyzed using AMIDE software. The mice were anesthetized with 5% isoflurane prior to each scan.

Dual-Targeted (Passive and Active) Tumor Accumulation.

The passive and synergistic passive/active targeting ability of this multimodal imaging agent (UCNPs@Tf-^{99m}Tc) was evaluated via T1-weighted MRI. Tumor-bearing mice were intravenously injected with cit-UCNP (without Tf coating, which only can reach the tumor area via passive targeting) and UCNPs@Tf-^{99m}Tc (with Tf coating, which can reach the tumor area via passive as well as Tf receptor-mediated active targeting). The MRI images were captured at different time intervals using a 7 T MRI scanner (PET/MR 7 T, BRUKER, Massachusetts, USA). The concentration of both cit-UCNP and UCNPs@Tf-^{99m}Tc was 1000 ppm, and the volume of the injection was 200 μ L per mouse. Prior to every scan, the mice were anesthetized with 5% isoflurane. Postinjection images were compared with pre-injection images of the respective mouse to evaluate the T1 contrast enhancement at the tumor site yielded by cit-UCNP and UCNPs@Tf-^{99m}Tc separately. The image reconstruction and analysis were performed using an open-source software AMIDE.

Multimodal Cancer Imaging In Vivo. Finally, the efficacy of UCNPs@Tf-^{99m}Tc under multiple in vivo imaging modalities was explored using MRI, SPECT/CT, IRTI, and CT. For MRI, a blank scan of a mouse was done followed by 200 μ L of UCNPs@Tf-^{99m}Tc (1000 ppm) tail vein injection and a second scan 2 h postinjection. The same protocol was followed for SPECT/CT imaging, where a separate mouse was scanned before, and 2 h post tail vein injection of 200 μ L of UCNPs@Tf-^{99m}Tc (196 μ Ci). For IRTI, the mice were

irradiated with 980 nm laser 2 h postinjection to capture the photothermal images using an IR thermal camera. For the CT scan, a microCT system (u-CT, MILabs, Netherlands) has been used. The mice were anesthetized with 5% isoflurane prior to each scan. MRI, SPECT, and CT images were analyzed using an open-source software AMIDE.

RESULTS AND DISCUSSION

Synthesis and Characterization of UCNP@Tf-^{99m}Tc Nanoformulation. Despite intense research, the current diagnostic techniques/methodologies fail to diagnose cancer early.³⁸ A nano-enabled multimodal imaging system offers multiple views with complementary characteristics. Two or more imaging modalities are combined to achieve detailed information of cancer progression by eliminating the intrinsic limitation of any individual modality.^{6,13,14,25} Various nano-material-based multimodal imaging has been reported before including UCNPs. For example, hyperbranched polymer (HBP) NPs functionalized with organic dye for MRI and optical imaging,³⁹ carbon-decorated ferrite nanodots (CDs@ MNFs) for fluorescence and MRI,⁶ UCNP-IONP-Au nanocomposite for MRI and UCL imaging,⁷ ¹²⁴I-labeled RGD-functionalized UCNPs for UCL, MR and PET imaging,²⁹ and a few more. However, these studies often suffer from unknown biocompatibility, poor bioavailability, and/or uncertain clearance and demonstrated targeting ability, in addition to limited imaging modalities. These drawbacks were all removed in the current design, where the human protein Tf was anchored on the surface of the NaGdF₄:Yb,Er NPs, and the protein cage is used for the chelation of the radioisotope.

The surfactant oleic acid (OA) on the surface of as-prepared core UCNPs was exchanged with citrate, allowing water dispersibility and apo-Tf (iron-free) conjugation via amide bonding. Finally, ^{99m}Tc was chelated into the free iron cage of the Tf protein to obtain the final UCNP@Tf-^{99m}Tc nanoformulation. The morphology of the as-synthesized OA-UCNP was studied using TEM and high-resolution (HR)-TEM (Figure 1a,b). The average diameter of the hexagonal OA-UCNPs was found to be 10 ± 3 nm and a lattice spacing of 0.5 nm (inset Figure 1b). The TEM analysis (Figure 1a,b) reveals the particle size, its distribution, and structure (hexagonal phase) that matched with those previously reported.^{20,21,34} The UV-vis absorption spectrum of Yb/Er-doped NaGdF₄:Yb,Er OA-UCNP (1 mg/mL in cyclohexene) shows absorption around ~978 nm (Figure 1c) matching previous reports.^{21,34} The power-dependent UCL from the as-synthesized OA-UCNPs under 980 nm excitation is shown in Figure 1d. The characteristic emission peaks of OA-UCNPs were observed at 520, 540, and 655 nm, and the intensity of UCL increases with incident power. The colloidal solution of the OA-UCNPs (1 mg/mL in cyclohexane) fluoresce predominantly green under the 980 nm excitation (inset Figure 1d). The UCL emission peaks of Er-doped OA-UCNPs at 520, 540, and 655 nm are due to the transitions from ²H_{11/2} to ⁴I_{15/2}, ⁴S_{3/2} to ⁴I_{15/2}, and ⁴F_{9/2} to ⁴I_{15/2}, respectively.^{20,21}

Figure 1e demonstrates the surface charge of different nanoformulations, as measured by the zeta potential. As-prepared OA-UCNP surfaces are positively charged (+49 mV) that switched to a negative (−18 mV) after the citrate functionalization. Such a drastic change in the zeta potential after the citrate functionalization is the primary indication of the ligand exchange. A further drop in the surface charge for UCNP@Tf (−24 mV) initially confirms the Tf conjugation.

The PDI (Figure S1) of OA-UCNP, cit-UCNP, and UCNP@Tf was found to be 0.295, 0.334, and 0.554, respectively. Additionally, the change in the hydrodynamic diameter (*D_h*) of the as-synthesized OA-UCNP, cit-UCNP, and UCNP@Tf also support Tf conjugation. Citrate functionalization on OA-UCNPs via ligand exchange resulted in a slight increase in *D_h*, which further increased after the Tf coating (Figure S2). This indirectly indicates the successful ligand exchange and Tf conjugation. The PDI represented the colloidal heterogeneity recorded from the photon correlation spectroscopic analysis, which was within the acceptable limit of 0.05–0.7.⁴⁰ The PDI values (Figure S1) show reasonably good monodispersity and homogenous size distribution of the composite and agrees with the TEM analysis (Figure 1a,b).

The further confirmation of the ligand exchange and the Tf conjugation can be found in Figure 1f, showing the FT-IR spectra of the nanoformulations at their different stages. For OA-UCNPs, absorption peaks at 3010, 2927, 2855, 1560, and 1465 cm^{−1} were observed. For OA-UCNPs, the absorption peak at 3010 cm^{−1} is attributed to the =C–H stretching vibration, and the peaks at 2927 and 2855 cm^{−1} arise from the asymmetric and symmetric stretching of methylene (CH₂), respectively, in the long alkyl chain of OA.⁴¹ Two peaks at 1560 and 1465 cm^{−1} correspond to the stretching vibrations of carboxylic (COO[−]) groups of OA.⁴¹ Post-citrate functionalization, the peak intensities at 2927 and 2855 cm^{−1} reduce significantly, and the peaks at 1560 and 1465 cm^{−1} shift to 1610 and 1450 cm^{−1}, respectively. The decrease in the OA-related peak intensity confirms the removal of OA.²⁰ Additionally, the shift in the COO[−] peaks to 1610 and 1450 cm^{−1}^{20,41} and a broadband near 3400 cm^{−1} indicate O–H stretching and confirm the successful citrate functionalization. After conjugating Tf with cit-UCNP, strong bands at 1650 and 1535 cm^{−1} associated with the amide I and amide II of Tf appear.⁴² The band at ~700 cm^{−1} can be assigned to the –NH₂ and –NH wagging in the Tf protein. The identification of the FT-IR absorption modes is given in Table S1. The approximate Tf conjugation on UCNPs was calculated using a similar formalism to estimate the drug loading efficiency in nanoparticle vectors.³⁶ The Tf loading efficiency was found to be ~6% using the absorption value of Tf at 280 nm.⁴³

Next, Tf works as a host for ^{99m}Tc chelation. SPECT imaging, one of the key modalities used here, depends critically on a stable chelation of ^{99m}Tc within the nanocomposite. The empty iron core of the conjugated Tf served as the chelation center for the radioisotope ^{99m}Tc, which has characteristic similarities with Fe⁴⁺³² to make the nanoformulation SPECT active. The radiolabeling efficiency and the stability of the ^{99m}Tc-chelated UCNP@Tf (UCNP@Tf-^{99m}Tc) were evaluated using radio thin-layer chromatography (radio-TLC), as depicted in Figure 2. The radio-chromatogram of the mobile free ^{99m}Tc (black dashed line, Figure 2a) moved ~65 mm vis-à-vis the UCNP@Tf-^{99m}Tc (blue dashed line, Figure 2a), which remained at the bottom (~25 mm position) of the TLC paper. The radiolabeling efficiency into UCNP@Tf was found to be >95%, matching previous reports.^{32,33}

The phase stability of UCNP@Tf-^{99m}Tc was examined in PBS at 4 and 37 °C to mimic the storage and injection conditions, in 20% serum at 37 °C to imitate the physiological environment. The dissociation of the ^{99m}Tc from the UCNP@Tf was observed for 48 h. As shown in Figure 2b, UCNP@Tf-^{99m}Tc taken in 20% serum at 37 °C shows no release of the ^{99m}Tc for the first 6 h. However, after 24 h, a 10 ± 2% (*n* = 3

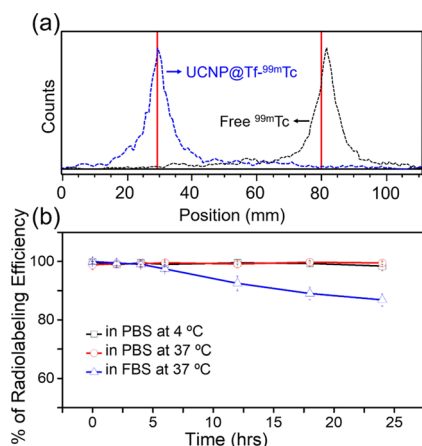


Figure 2. (a) Radio-chromatogram of free ^{99m}Tc and UCNP@Tf- ^{99m}Tc . (b) In vitro radiochemical stability (measured with radio-TLC) of UCNP@Tf- ^{99m}Tc in different conditions (4 °C in PBS, 37 °C in PBS, and 37 °C in FBS).

experiments) release of the radioisotope from the UCNP@Tf- ^{99m}Tc was observed. When the UCNP@Tf- ^{99m}Tc is incubated in PBS at 4, and 37 °C, no measurable release of the ^{99m}Tc radiolabel could be observed until 24 h, indicating $\sim 100\%$ ($n = 3$ experiments) phase stability of the nano-composite. Such stability, $>90\%$ over 24 h in all conditions, is ideal for in vivo applications.^{32,33}

In Vitro Examinations. The cytotoxicity and intracellular distribution of the nanoformulation were investigated on 4 T1 breast cancer cell line by conventional MTT assay and CLSM, respectively. A viability in excess of 75% is generally considered as nontoxic.⁴⁴ The MTT assay revealed that $>75\%$ 4 T1 cells are viable even at high concentrations (1000 ppm) of UCNP@

Tf (Figure 3a) or UCNP@Tf- ^{99m}Tc (Figure 3b), suggesting our nanoformulations to be nontoxic and biocompatible. To be on the safe side, we have chosen 500 ppm ($>80\%$ cell viability, Figure 3a,b) for further in vitro studies. Only at 2000 ppm concentration, the cell viability decreases to $\sim 50\%$. A similar outcome has been previously reported using differently functionalized UCNPs, which showed low cytotoxicity even at higher concentrations^{20,24,34} when compared with other metallic nanoparticles⁴⁵ and quantum dots.⁴⁶ We have previously reported a viability in excess of 80% for UCNP incubated 3 T3 derived fat cells (normal cells).³⁴ This shows the potential of the UCNP-based composites for biomedical applications, where toxicity is a major limiting factor. Cells treated with UCNP@Tf- ^{99m}Tc nanoformulation and co-stained with DAPI, a nucleus staining dye, was subjected to CLSM to examine the endocytosis and intracellular distribution. Upon 405 nm excitation, bright blue emission at 461 nm (Figure 3c, panel ii) was observed from the nucleus, while the cell cytoplasm emitted the UCNP signal at 540 nm (Figure 3c, panel iii) when irradiated with 980 nm light. The green UCL (at 540 nm) originated from the UCNPs upon 980 nm excitation proving UCNP@Tf internalization and intracellular distribution in the cytoplasm (Figure 3c, overlay image in panel iv).

Prior to the in vivo evaluation, pentamodality of the nanoformulation (UCNP@Tf- ^{99m}Tc) was examined in vitro, using a concentration-dependent phantom (Figure 4). Figure 4a demonstrates the photothermal temperature elevation in the colloidal solutions, with increasing concentrations of UCNP@Tf- ^{99m}Tc , upon laser irradiation (0.32 W/cm^2 for 7.5 min) in comparison to pure water (0 ppm). The final temperature of well (i) containing only water (0 ppm) was $\sim 33^\circ\text{C}$, whereas the temperature of the well (v) containing 800 ppm UCNP@Tf- ^{99m}Tc increased above 40°C under

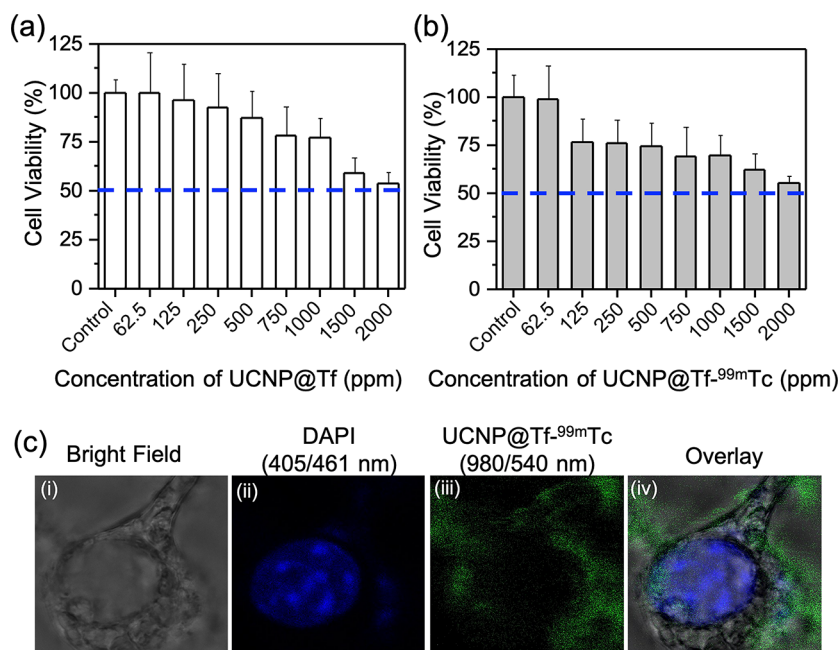


Figure 3. In vitro MTT cytotoxicity assays of concentration-dependent (a) UCNP@Tf and (b) UCNP@Tf- ^{99m}Tc on 4 T1 breast cancer cells treated for 24 h. Control indicates untreated cells. Data are presented as mean \pm SD, with the number of repetitions $n = 5$. The horizontal dashed blue line in (a,b) indicates 50% cell viability. (c) Confocal microscope images of DAPI-stained 4 T1 cells treated with UCNP@Tf (500 ppm). (i) Bright field, (ii) 461 nm DAPI fluorescence from the nucleus under 405 nm excitation; (iii) UCL of UCNP@Tf- ^{99m}Tc at 540 nm upon 980 nm excitation; (iv) overlay.

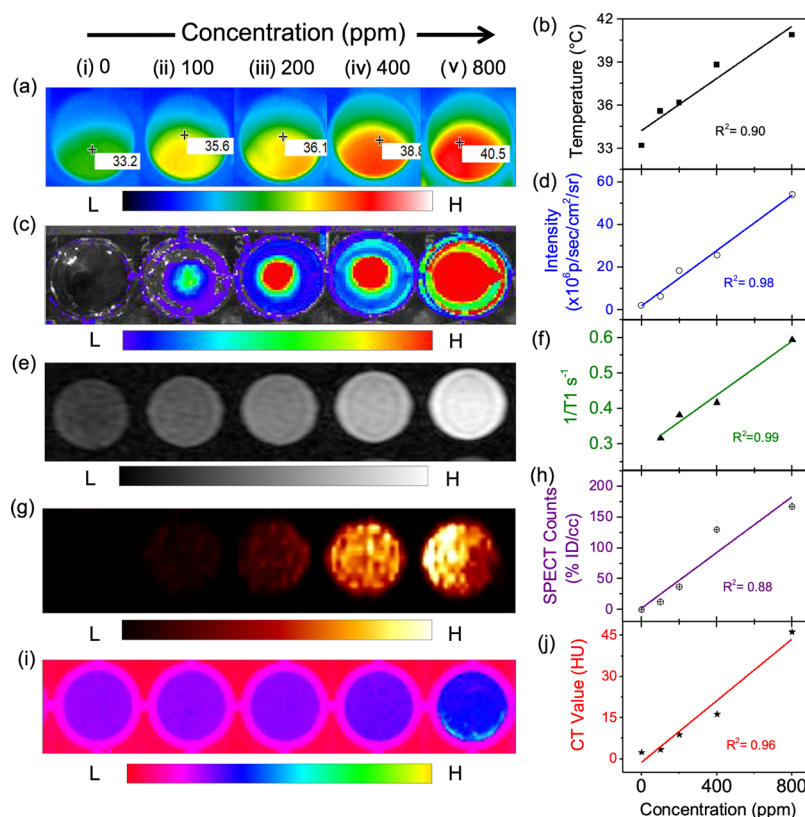


Figure 4. In vitro pentamodal imaging of UCNPs@Tf-^{99m}Tc. Image and the concentration-dependent (0, 100, 200, 400, and 800 ppm) signal changes under (a,b) IRTI, (c,d) IVIS, (e,f) T1-weighted MRI, (g,h) SPECT, and (i,j) CT, respectively. The color coding for each study is presented with each panel. (b,d,f,h,j) represents the variation of respective signal intensity as a function of agent concentration under IRTI, IVIS, MRI, SPECT, and CT, respectively. The line joining the data points is a linear fit to the data with specific correlation coefficients mentioned. For IRTI and IVIS, the phantom was irradiated with 980 nm laser; UCL under IVIS was recorded in the GFP window (~500 to 550 nm).

identical irradiation conditions. The saturated equilibrium temperature obtained from each well is plotted as a function of the agent concentration (Figure 4b). The photothermal temperature increase of ~7 °C in the well (i) containing only water is due to 980 nm absorption in water,⁴⁷ and a further increase in temperature in the other wells (ii–v) is solely attributed to the photothermal agent UCNPs in the UCNPs@Tf-^{99m}Tc nanoformulation (Figure 4a,b). The temporal rise of the temperature in the solutions can be found in Figure S3. This elevated temperature at high concentrations of the agent can be utilized for thermal imaging and photothermal therapy.^{21,34} UCNPs have demonstrated photothermal conversion efficiency (η) > 60%^{21,34} via nonradiative relaxations in the emitter Er (Figure S4) and lattice vibrations in the crystalline host.⁴⁸

A similar data presentation was adopted for the successive panels showing other modalities (Figure 4c–j). The UCL intensities of the UCNPs@Tf-^{99m}Tc were found to be increasing linearly with the agent concentration (Figure 4c,d). The concentration-dependent UCL image (Figure 4c) acquired by IVIS under 980 nm irradiation and its variation with the probe concentration (Figure 4d) demonstrate the efficiency of UCNPs@Tf-^{99m}Tc for small animal imaging under a low irradiation dose. The average radiant efficiency of 6.5×10^4 p/s/cm²/sr per mM follows the pattern of other reported inorganic nanoparticles as an optical imaging agent such as carbon-decorated ferrite nanodots.⁶ The excellent regression of 0.98 (Figure 4d) from IVIS, and the deep penetrating³⁴ NIR excitation (Figure 4d), in addition to the known long-lasting

photostability²¹ of the UCNPs, makes the UCNPs@Tf-^{99m}Tc nanocomposite a superior optical imaging agent. A comparison of spectral (Fluorolog) and imaged (IVIS) UCL properties of the UCNPs@Tf-^{99m}Tc nanoformulation are depicted in Figure S5.

Figure 4e,f demonstrates the positive correlation of the MR signal with the increasing concentration of UCNPs@Tf-^{99m}Tc dispersed in water. The T1-weighted MR signal intensity (SI) increased with the concentration of the UCNPs@Tf-^{99m}Tc (Figure 4e). Such contrast was attributed to the Gd dopant in the UCNPs.^{23,24} The higher concentration, thus higher Gd, resulted in stronger MR SI, and hence, brighter images. To quantify the T1-weighted contrast of the UCNPs@Tf-^{99m}Tc, longitudinal relaxivity ($r_1 = 1/T_1$) values were computed by obtaining T1 FLAIR images with variable T1 (400–2000 ms). The relaxivity value (r_1) of the UCNPs@Tf-^{99m}Tc nanoformulation is found to be 0.38 mL mg^{−1} s^{−1}. The variation of the $1/T_1$ value as a function of probe concentration is plotted in Figure 4f. The maximum $1/T_1$ enhancement was approximately two-fold compared to the reference (water), confirming the contribution of the Gd³⁺ ions. Notably, we found that the MR signal had a linear correlation up to 1600 ppm of UCNPs@Tf-^{99m}Tc, and any further increase in the concentration leads to a reduction in the MR signals (Figure S6) due to the T2-shortening effect, also known as T_2^* -related signal loss at high concentrations of Gd.⁴⁹

Figure 4g,h shows the in vitro phantom SPECT image and the relative SPECT counts versus the concentration of UCNPs@Tf-^{99m}Tc, respectively. The SPECT image (Figure

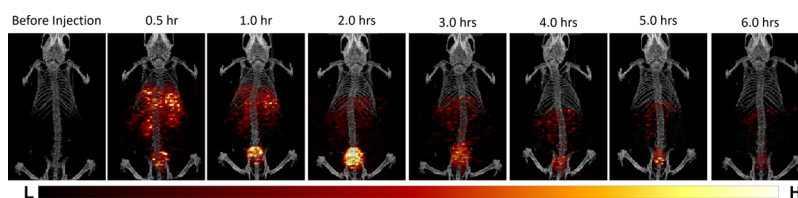


Figure 5. In vivo pharmacokinetics of the UCNP@Tf- ^{99m}Tc by overlaid SPECT/CT imaging. Color-coded SPECT images of healthy mice (BALB/C; 6–8 weeks old) before, and 0.5, 1.0, 2.0, 3.0, 4.0, 5.0, and 6.0 h post-injection of UCNP@Tf- ^{99m}Tc (intravenous; 200 μL : 1000 ppm; 180 μCi).

4g) and the concentration dependence plot (Figure 4h) demonstrate the linear variation of SPECT signals with increasing agent concentration similar to all other modalities, albeit with a low regression value of 0.88. Sun et al. reported UCNP-based multimodal imaging agent demonstrating SPECT by forming a shell of $^{153}\text{Sm}^{3+}$ -doped NaGdF_4 on the $\text{NaLuF}_4\text{:Yb,Tm}$ UCNPs.⁵⁰ As a result, the nanoagent is radioactive as-grown and requires specialized radio-handling expertise for all the formulation/characterization steps, as well as during imaging under other modalities. Our nanoformulation offers safe nonradioactive tetramodal imaging, which can be radiolabeled on site “on-site” and “on-demand”.

Apart from the thermal, UCL, MR and SPECT, the 980 nm absorber Yb ions used in the UCNPs provide CT contrast.²⁴ Our data reveal that the Yb ion-containing UCNP@Tf- ^{99m}Tc can produce reasonable CT contrast (Figure 4i), resulting in positive correlation between agent concentrations and CT values (HU) (Figure 4j). Similar findings have been reported before.^{23,24} The remarkable sensitivity and consistency of UCNP@Tf- ^{99m}Tc under all these five modalities prove the potential of this smart contrast agent to be used for actively targeted in vivo multimodal bioimaging.

Biodistribution, Cancer Targeting, and Multimodal Cancer Imaging. The biodistribution assessment of a nanoagent is essential to evaluate its bioavailability and clearance behavior.⁵¹ The biodistribution characteristics of the IV-injected UCNP@Tf- ^{99m}Tc in the mouse model was examined under SPECT/CT (Figure 5). The SPECT/CT images captured at different points in time revealed the initial biodistribution of the UCNP@Tf- ^{99m}Tc nanocomposites and later translocation in the mouse. UCNP@Tf- ^{99m}Tc accumulates in the liver, kidneys, and bladder shortly after injection. The high accumulation/uptake in the liver is a general result for most NPs, but in this case, the effect may be compounded by the increased expression of TfR in liver cells and the affinity of the UCNP@Tf- ^{99m}Tc toward the Kupffer cells of the liver.⁵² A progressive reduction in radioactivity from the liver and kidney, while increase in the bladder, suggests renal clearance of UCNP@Tf- ^{99m}Tc nanoformulation.^{32,53} Post 6 h injection, a low residual radioactivity was found throughout the body. The radioactivity in the bladder remained at high levels throughout the experiments. The images were duly compensated to account for the decay of the radioisotope, and the signal is only proportional to the accumulation of the UCNP@Tf- ^{99m}Tc nanocomposites. Previous reports demonstrated a range of clearance time, for example, 6–12 h for RBC-FA-UCNPs,⁵⁴ 8–24 h for carboxyl-functionalized UCNPs,⁵⁵ and >48 h for ^{153}Sm -doped UCNPs.⁵⁰ Such disparities only indicate that nanoparticle clearance depends on several factors, for instance, the composition, size, surface charge and its value, and so on.⁵⁶ The biodistribution behavior of the UCNP@Tf- ^{99m}Tc , here, closely matches with a recent report using

RBC-FA-UCNPs (folic acid functionalized red blood cell membrane coated UCNPs) examined under IVIS and PET.⁵⁴ The faster clearance observed here may be a result of the Tf biofunctionalization, as obtained for the RBC-coated UCNPs previously.⁵⁴ Other factors such as the small size, uniform dispersion (less agglomeration), surface charge type, and value due to Tf conjugation may also contribute to the lower clearance time.

Satisfactory in vivo biodistribution of the nanoformulation encourages us to examine the passive only, and both active and passively targeted tumor (tumor growth curve shown in Figure S7) accumulation without and with Tf, respectively. Nanoparticles with sizes ranging from 10 to 500 nm are known to be suitable for EPR-mediated tumor accumulation, also known as passive targeting.⁵⁶ The cit-UCNPs with a hydrodynamic diameter of ~ 140 nm (Figure S2) would qualify for EPR-mediated passive targeting⁵⁷ and enhance the MR contrast at the tumoral area. On the other hand, the cit-UCNP@Tf demonstrates stronger MR contrast because of EPR-mediated passive targeting, having a hydrodynamic diameter of ~ 231 nm (Figure S2) and also TfR-mediated active targeting of cancer.^{30–32} Figure 6a (top panel) shows the gradual increase in the MR signal at the tumoral area, confirming the EPR-mediated passive tumor targeting.⁵⁷ As expected, the MR contrast for the mice receiving the UCNP@Tf- ^{99m}Tc was significantly higher (bottom panel, Figure 6a), confirming synergistic active and passive targeted accumulation. A similar approach has been employed by Fang et al., where bare UCNPs have been used to describe the passive targeting and CC_{m231} (cancer cell membrane)-coated UCNPs for combined passive and homologous-targeting of MDA-MB-231 cancer.⁵⁸

Additionally, we have calculated the ΔSNR values (signal-to-noise ratio = signal of tumor/signal of background; Figure 6b) from the MR images to confirm our finding quantitatively. The ΔSNR values for nanocomposites with and without Tf were ~ 8.6 and ~ 3.89 , respectively, supporting our claim. The MRI-SNR-driven evaluation of active cancer-targeting has also been reported to examine the accumulation of the RGD-peptide functionalized UCNPs in U87MG tumors.²⁹ However, this particular study focused on targeting a specific type of cancer (U87MG).²⁹ In our study, the use of Tf enables targeting a wide range of cancer^{30,59} and also makes the nanoagent (UCNP@Tf- ^{99m}Tc) immune friendly as it is derived from the human body.^{30,31,59} UCNPs functionalized with folic acid (FA), which has their own drawback,⁶⁰ have been reported for active targeting of various cancers.⁶¹

Finally, UCNP@Tf- ^{99m}Tc nanoformulations were used for in vivo cancer imaging under MRI, SPECT, CT, and IRTI, and presented in Figure 7a–d. Figure 7a showcases the weak and strong MR contrast of the 4 T1 tumor bearing mice before (top panel) and after (bottom panel) the intravenous injection of the UCNP@Tf- ^{99m}Tc . Within 2 h of the injection, a

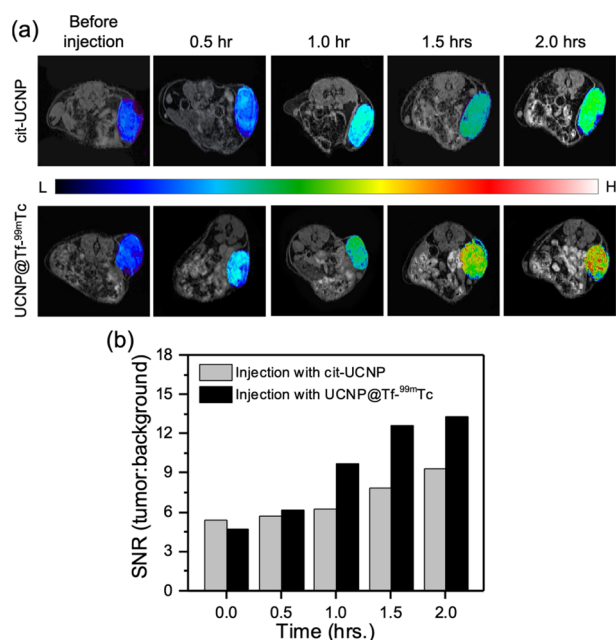


Figure 6. (a) T1-weighted MR images of tumor-bearing mice intravenously injected with cit-UCNP or UCNPs@Tf-^{99m}Tc (200 μ L; 1000 ppm in PBS) acquired at different time intervals (before injection, and 0.5–2.0 h post-injection). The tumor sites are color-coded for clarity of the contrast-enhancing effects of Gd-containing cit-UCNP and UCNPs@Tf-^{99m}Tc with targeting agent Tf. (b) Bar diagram demonstrates the changes in the SNR as a function of the injection time of cit-UCNP and UCNPs@Tf-^{99m}Tc.

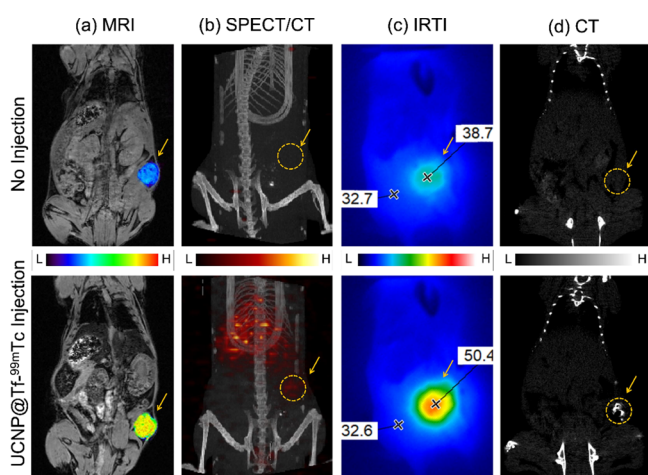


Figure 7. In vivo cancer imaging under different modalities: (a) MRI, (b) SPECT/CT, (c) IRTI, and (d) CT, before and after intravenous injection (2 h) of UCNPs@Tf-^{99m}Tc. The tumor area in MR images (a) are color-coded for clarity. The yellow arrows indicate the tumor position, and the area encircled by yellow dashed lines in (b) and (d) show the approximate outline of the tumor.

significant increase in the MR signal was observed in the tumoral area (color coded for clarity), and a detectable positive contrast in the liver (Figure 7a, bottom panel) also. Biodistribution studies with MRI is limited as nontargeted anatomical features also produced significant MR contrast in both images that resulted in a poor SNR.⁶² SPECT/CT imaging (Figure 7b), on the other hand, shows complete absence of contrast (Figure 7b, top panel) and clear accumulation of the UCNPs@Tf-^{99m}Tc nanoformulation in

the tumoral area (Figure 7b, bottom panel) as well as its distribution throughout the body.^{2,10} This set of data proves how multimodal imaging could combine the strengths of MRI^{4,58} and excellent sensitivity of SPECT^{2,10} for efficient cancer theranostics. The use of UCNPs@Tf-^{99m}Tc provides the synergy of these two modalities to achieve better resolution per unit dosage.

Additionally, the injection of UCNPs@Tf-^{99m}Tc nanoformulation increased the local photothermal temperature at the tumor site by ~ 18 $^{\circ}$ C (Figure 7c bottom panel), compared to only ~ 6 $^{\circ}$ C (Figure 7c top panel) caused by the irradiation only. The additional increase of 12 $^{\circ}$ C in the tumor with the nanoformulation under 0.32 W/cm² for 7.5 min is superior to that reported earlier as 20 $^{\circ}$ C under 0.75 W/cm² for 10 min.⁶³ Furthermore, we examined the Yb component in UCNPs@Tf-^{99m}Tc-mediated CT contrast in vivo (Figure 7d). As depicted, the CT value at the tumor site was significantly increased after the UCNPs@Tf-^{99m}Tc injection (761.6 HU) (bottom panel, Figure 7d) than without the injection (35.2 HU) (top panel, Figure 7d). Ruichan et al. has reported the highest HU of 447.5 at the tumoral site after the injection of UCNPs@mSiO₂-Dopa.²³ In another study, GO/ZnFe₂O₄/UCNPs reported an increase in the CT value by 274 HU at the tumoral site post-injection.²⁴ The offered imaging modalities overcome their individual intrinsic limitations when used in combination. For example, T1-weighted MRI provided the soft-tissue contrast, whereas the SPECT/CT and UCL offered the deep tissue imaging capabilities. CT images unfold the high-resolution tissue characteristics, which renders volumetric imaging of the organs and tumor possible. The photothermal imaging using IRTI offers a simple alternative to image the tumor. In addition, UCNPs@Tf-^{99m}Tc nanoformulation is proven to exhibit excellent cancer targeting ability along with superior biocompatibility and near-ideal biodistribution.

CONCLUSIONS

In summary, we offer a single upconversion nanoformulation, UCNPs@Tf-^{99m}Tc, for synergetic dual-targeted (passive and active) pentamodal cancer imaging in vitro and in vivo and demonstrating near-ideal renal clearance. The imaging modalities include infrared thermal imaging, IVIS, MRI, SPECT, and CT. The 980 nm excitation in the biological transparency window provided the radiative UCL, while the Gd and Yb ion constituents of the UCNPs provided the MR and CT contrast, respectively. The nonradiative recombination in the UCNPs generated the photothermal heat for thermal contrast imaging. The magnetic UCNPs are covalently conjugated with human Tf protein for active targeting and stealth, which doubles up as home to the radiolabel ^{99m}Tc (radiolabeling efficiency = 95–100%) with excellent stability for SPECT imaging. The in vitro experimental results, including confocal laser scanning microscopy, validate easy cellular uptake and excellent biocompatibility of the nanoformulation within the linear regime of respective signal variations as a function of concentration. The in vivo SPECT/CT imaging showed efficient renal clearance within 6 h. In vivo MRI reveals the passive and active T1 cancer-targeting ability of the UCNPs@Tf-^{99m}Tc. An actively targeted, stable, and biocompatible upconversion nanoformulation for penta-modal imaging is demonstrated that offers safe renal clearance, which is a requirement for clinical application.

■ ASSOCIATED CONTENT

SI Supporting Information

The Supporting Information is available free of charge at <https://pubs.acs.org/doi/10.1021/acsanm.2c01016>.

PDI analysis of different nanocomposites; hydrodynamic diameter of different nanocomposites; concentration-dependent photothermal ability of UCNPs@Tf-^{99m}Tc nanocomposites; schematic energy-level diagrams of the UCL mechanism for the NaGdF₄:Yb,Er nanoparticles; performance comparison of UCNPs@Tf-^{99m}Tc nanocomposites under Fluorolog Tau 3 and IVIS; concentration-dependent T1-weighted MR contrast measurement under the 7 T MRI system, and tumor growth curve (PDF)

■ AUTHOR INFORMATION

Corresponding Author

Surojit Chattopadhyay – Institute of Biophotonics, National Yang-Ming Chiao Tung University, Taipei 112, Taiwan; orcid.org/0000-0002-1384-3379; Email: sur@nycu.edu.tw

Authors

Najim Akhtar – Institute of Biophotonics, National Yang-Ming Chiao Tung University, Taipei 112, Taiwan; orcid.org/0000-0001-9975-7537

Pei-Wen Wu – Department of Biomedical Imaging and Radiological Sciences, National Yang Ming Chiao Tung University, Taipei 112, Taiwan; orcid.org/0000-0002-1912-0227

Chuan Lin Chen – Department of Biomedical Imaging and Radiological Sciences, National Yang Ming Chiao Tung University, Taipei 112, Taiwan

Wen-Yi Chang – National PET/Cyclotron Center, Nuclear Medicine Department, Taipei Veterans General Hospital, Taipei 112, Taiwan; orcid.org/0000-0003-2409-3814

Ren-Shyan Liu – Department of Biomedical Imaging and Radiological Sciences, National Yang Ming Chiao Tung University, Taipei 112, Taiwan; National PET/Cyclotron Center, Nuclear Medicine Department, Taipei Veterans General Hospital, Taipei 112, Taiwan

Chien Ting Wu – Nano Device Materials Characterization Division, National Nano Device Laboratories, Hsinchu 300, Taiwan; orcid.org/0000-0003-2220-3696

Agnishwar Girigoswami – Faculty of Allied Health Sciences, Chettinad Hospital & Research Institute (CHRI), Chettinad Academy of Research and Education (CARE), Chennai 603103, India; orcid.org/0000-0003-0475-2544

Complete contact information is available at: <https://pubs.acs.org/doi/10.1021/acsanm.2c01016>

Author Contributions

N.A.: conceptualization, visualization, methodology, investigation, data curation, formal analysis, validation, and writing – original draft; P.-W.W.: assistance in investigation; C.L.C.: resources, and writing – review and editing; W.-Y.C.: assistance in investigation; R.-S.L.: resources and validation; C.T.W.: assistance in investigation; A.G.: resources, validation, and writing – review and editing; S.C.: supervision, resources, funding acquisition, visualization, project administration, methodology, validation, and writing – review and editing.

Notes

The authors declare no competing financial interest.

■ ACKNOWLEDGMENTS

The authors acknowledge financial support from the Ministry of Science and Technology (MOST), Taiwan, under grant # 107-2112-M-010-003-MY3. The authors acknowledge support from Taipei Veterans General Hospital PET Centre and the technicians for specific imaging services. Mohammed Bouras of Functional Nanomaterials Laboratory is acknowledged for helping with the figure design.

■ REFERENCES

- (1) Amoroso, A. J.; Pope, S. J. Using lanthanide ions in molecular bioimaging. *Chem. Soc. Rev.* **2015**, *44*, 4723–4742.
- (2) Pimlott, S. L.; Sutherland, A. Molecular tracers for the PET and SPECT imaging of disease. *Chem. Soc. Rev.* **2011**, *40*, 149–162.
- (3) Wallyn, J.; Anton, N.; Akram, S.; Vandamme, T. F. Biomedical imaging: principles, technologies, clinical aspects, contrast agents, limitations and future trends in nanomedicines. *Pharm. Res.* **2019**, *36*, 78.
- (4) Bowtell, R. Colourful future for MRI. *Nature* **2008**, *453*, 993–994.
- (5) Miles, K. Functional computed tomography in oncology. *Eur. J. Cancer* **2002**, *38*, 2079–2084.
- (6) Sharmiladevi, P.; Akhtar, N.; Haribabu, V.; Girigoswami, K.; Chattopadhyay, S.; Girigoswami, A. Excitation wavelength independent carbon-decorated ferrite nanodots for multimodal diagnosis and stimuli responsive therapy. *ACS Appl. Bio Mater.* **2019**, *2*, 1634–1642.
- (7) Cheng, L.; Yang, K.; Li, Y.; Chen, J.; Wang, C.; Shao, M.; Lee, S. T.; Liu, Z. Facile preparation of multifunctional upconversion nanoprobe for multimodal imaging and dual-targeted photothermal therapy. *Angew. Chem., Int. Ed. Engl.* **2011**, *50*, 7385–7390.
- (8) Smith-Bindman, R. Is computed tomography safe. *N. Engl. J. Med.* **2010**, *363*, 1–4.
- (9) Ahmed, H. U.; Kirkham, A.; Arya, M.; Illing, R.; Freeman, A.; Allen, C.; Emberton, M. Is it time to consider a role for MRI before prostate biopsy? *Nat. Rev. Clin. Oncol.* **2009**, *6*, 197–206.
- (10) Bateman, T. M. Advantages and disadvantages of PET and SPECT in a busy clinical practice. *J. Nucl. Cardiol.* **2012**, *19*, 3–11.
- (11) Ai, X.; Mu, J.; Xing, B. Recent advances of light-mediated theranostics. *Theranostics* **2016**, *6*, 2439.
- (12) Lee, S. Y.; Jeon, S. I.; Jung, S.; Chung, I. J.; Ahn, C.-H. Targeted multimodal imaging modalities. *Adv. Drug Delivery Rev.* **2014**, *76*, 60–78.
- (13) Lee, D.-E.; Koo, H.; Sun, I.-C.; Ryu, J. H.; Kim, K.; Kwon, I. C. Multifunctional nanoparticles for multimodal imaging and theragnosis. *Chem. Soc. Rev.* **2012**, *41*, 2656–2672.
- (14) Bouzas-Ramos, D.; Cigales Canga, J.; Mayo, J. C.; Sainz, R. M.; Ruiz Encinar, J.; Costa-Fernandez, J. M. Carbon quantum dots codoped with nitrogen and lanthanides for multimodal imaging. *Adv. Funct. Mater.* **2019**, *29*, No. 1903884.
- (15) Von Maltzahn, G.; Park, J.-H.; Agrawal, A.; Bandaru, N. K.; Das, S. K.; Sailor, M. J.; Bhatia, S. N. Computationally guided photothermal tumor therapy using long-circulating gold nanorod antennas. *Cancer Res.* **2009**, *69*, 3892–3900.
- (16) Hsu, J. C.; Naha, P. C.; Lau, K. C.; Chhour, P.; Hastings, R.; Moon, B. F.; Stein, J. M.; Witschey, W. R.; McDonald, E. S.; Maidment, A. D. An all-in-one nanoparticle (AION) contrast agent for breast cancer screening with DEM-CT-MRI-NIRF imaging. *Nanoscale* **2018**, *10*, 17236–17248.
- (17) Chen, F.; Zhao, E. R.; Hableel, G.; Hu, T.; Kim, T.; Li, J.; Gonzalez-Pech, N. I.; Cheng, D. J.; Lemaster, J. E.; Xie, Y. Increasing the efficacy of stem cell therapy via triple-function inorganic nanoparticles. *ACS Nano* **2019**, *13*, 6605–6617.
- (18) Shi, H.; Yan, R.; Wu, L.; Sun, Y.; Liu, S.; Zhou, Z.; He, J.; Ye, D. Tumor-targeting CuS nanoparticles for multimodal imaging and

guided photothermal therapy of lymph node metastasis. *Acta Biomater.* **2018**, *72*, 256–265.

(19) Vogelsang, J.; Kasper, R.; Steinhauer, C.; Person, B.; Heilemann, M.; Sauer, M.; Tinnefeld, P. A reducing and oxidizing system minimizes photobleaching and blinking of fluorescent dyes. *Angew. Chem., Int. Ed.* **2008**, *47*, 5465–5469.

(20) Ghosh, S.; Chang, Y.-F.; Yang, D.-M.; Chattopadhyay, S. Upconversion nanoparticle-mOrange protein FRET nanoprobe for self-ratiometric/ratiometric determination of intracellular pH, and single cell pH imaging. *Biosens. Bioelectron.* **2020**, *155*, No. 112115.

(21) Thakur, M. K.; Gupta, A.; Ghosh, S.; Chattopadhyay, S. Graphene-Conjugated Upconversion Nanoparticles as Fluorescence-Tuned Photothermal Nanoheaters for Desalination. *ACS Appl. Nano Mater.* **2019**, *2*, 2250–2259.

(22) Dibaba, S. T.; Wei, R.; Xi, W.; Zhao, L.; Shi, L.; Ren, W.; Mayr, T.; Sun, L. Theranostic nanocomposite from upconversion luminescent nanoparticles and black phosphorus nanosheets. *RSC Adv.* **2018**, *8*, 35706–35718.

(23) Lv, R.; Yang, P.; Chen, G.; Gai, S.; Xu, J.; Prasad, P. N. Dopamine-mediated photothermal theranostics combined with up-conversion platform under near infrared light. *Sci. Rep.* **2017**, *7*, 1–13.

(24) Bi, H.; He, F.; Dai, Y.; Xu, J.; Dong, Y.; Yang, D.; Gai, S.; Li, L.; Li, C.; Yang, P. Quad-model imaging-guided high-efficiency phototherapy based on upconversion nanoparticles and ZnFe₂O₄ integrated graphene oxide. *Inorg. Chem.* **2018**, *57*, 9988–9998.

(25) Du, B.; Cao, X.; Zhao, F.; Su, X.; Wang, Y.; Yan, X.; Jia, S.; Zhou, J.; Yao, H. Multimodal imaging-guided, dual-targeted photothermal therapy for cancer. *J. Mater. Chem. B* **2016**, *4*, 2038–2050.

(26) Generalova, A.; Rocheva, V.; Nechaev, A.; Khochkov, D.; Sholina, N.; Semchishen, V.; Zubov, V.; Koroleva, A.; Chichkov, B.; Khaydukov, E. PEG-modified upconversion nanoparticles for in vivo optical imaging of tumors. *RSC Adv.* **2016**, *6*, 30089–30097.

(27) Liu, J.-N.; Bu, W.-B.; Shi, J.-L. Silica coated upconversion nanoparticles: a versatile platform for the development of efficient theranostics. *Acc. Chem. Res.* **2015**, *48*, 1797–1805.

(28) Jang, J. Y.; Lee, D. Y.; Park, S. J.; Byun, Y. Immune reactions of lymphocytes and macrophages against PEG-grafted pancreatic islets. *Biomaterials* **2004**, *25*, 3663–3669.

(29) Lee, J.; Lee, T. S.; Ryu, J.; Hong, S.; Kang, M.; Im, K.; Kang, J. H.; Lim, S. M.; Park, S.; Song, R. RGD peptide–conjugated multimodal NaGdF₄: Yb³⁺/Er³⁺ nanophosphors for upconversion luminescence, MR, and PET imaging of tumor angiogenesis. *J. Nucl. Med.* **2013**, *54*, 96–103.

(30) Brandsma, M. E.; Jevnikar, A. M.; Ma, S. Recombinant human transferrin: beyond iron binding and transport. *Biotechnol. Adv.* **2011**, *29*, 230–238.

(31) Wang, D.; Zhu, L.; Pu, Y.; Wang, J.-X.; Chen, J.-F.; Dai, L. Transferrin-coated magnetic upconversion nanoparticles for efficient photodynamic therapy with near-infrared irradiation and luminescence bioimaging. *Nanoscale* **2017**, *9*, 11214–11221.

(32) Gu, B.; Cai, J.; Zhang, J.; Xu, X.; Luo, J.; Zhou, X.; Zheng, Y.; Zhang, Y. 99m Tc-labeled and gadolinium-chelated transferrin enhances the sensitivity and specificity of dual-modality SPECT/MR imaging of breast cancer. *RSC Adv.* **2016**, *6*, 20532–20541.

(33) Harris, W. R.; Chen, Y.; Wein, K. Equilibrium constants for the binding of indium (III) to human serum transferrin. *Inorg. Chem.* **1994**, *33*, 4991–4998.

(34) Gupta, A.; Lam, C. W.; Wu, C. T.; Yang, D. M.; Chattopadhyay, S. Photothermal disintegration of 3T3 derived fat droplets by irradiated silica coated upconversion nanoparticles. *Part. Part. Syst. Charact.* **2018**, *35*, No. 1800294.

(35) Wang, D.; Chen, C.; Ke, X.; Kang, N.; Shen, Y.; Liu, Y.; Zhou, X.; Wang, H.; Chen, C.; Ren, L. Bioinspired near-infrared-excited sensing platform for in vitro antioxidant capacity assay based on upconversion nanoparticles and a dopamine–melanin hybrid system. *ACS Appl. Mater. Interfaces* **2015**, *7*, 3030–3040.

(36) Gomes, M. J.; Martins, S.; Ferreira, D.; Segundo, M. A.; Reis, S. Lipid nanoparticles for topical and transdermal application for alopecia treatment: development, physicochemical characterization,

and in vitro release and penetration studies. *Int. J. Nanomed.* **2014**, *9*, 1231.

(37) Kao, F.-H.; Akhtar, N.; Chen, C.-C.; Chen, H. Y.; Thakur, M. K.; Chen, Y.-Y.; Chen, C.-L.; Chattopadhyay, S. In Vivo and in Vitro Demonstration of Gold Nanorod Aided Photothermal Presoftening of B16F10 Melanoma for Efficient Chemotherapy Using Doxorubicin Loaded Graphene Oxide. *ACS Appl. Bio Mater.* **2018**, *2*, 533–543.

(38) Luo, H.; Hernandez, R.; Hong, H.; Graves, S. A.; Yang, Y.; England, C. G.; Theuer, C. P.; Nickles, R. J.; Cai, W. Noninvasive brain cancer imaging with a bispecific antibody fragment, generated via click chemistry. *Proc. Natl. Acad. Sci. U. S. A.* **2015**, *112*, 12806–12811.

(39) Rolfe, B. E.; Blakey, I.; Squires, O.; Peng, H.; Boase, N. R.; Alexander, C.; Parsons, P. G.; Boyle, G. M.; Whittaker, A. K.; Thurecht, K. J. Multimodal polymer nanoparticles with combined 19F magnetic resonance and optical detection for tunable, targeted, multimodal imaging in vivo. *J. Am. Chem. Soc.* **2014**, *136*, 2413–2419.

(40) Danaei, M.; Dehghankhold, M.; Ataie, S.; Hasanzadeh Davarani, F.; Javanmard, R.; Dokhani, A.; Khorasani, S.; Mozafari, M. Impact of particle size and polydispersity index on the clinical applications of lipidic nanocarrier systems. *Pharmaceutics* **2018**, *10*, 57.

(41) Zhou, J.; Yu, M.; Sun, Y.; Zhang, X.; Zhu, X.; Wu, Z.; Wu, D.; Li, F. Fluorine-18-labeled Gd³⁺/Yb³⁺/Er³⁺ co-doped NaYF₄ nanophosphors for multimodality PET/MR/UCL imaging. *Biomaterials* **2011**, *32*, 1148–1156.

(42) Kowalczyk, A.; Matysiak-Brynda, E.; Bystrzejewski, M.; Sutherland, D. S.; Stojek, Z.; Nowicka, A. M. Conformational control of human transferrin covalently anchored to carbon-coated iron nanoparticles in presence of a magnetic field. *Acta Biomater.* **2016**, *45*, 367–374.

(43) Wang, K.; Zhang, Y.; Wang, J.; Yuan, A.; Sun, M.; Wu, J.; Hu, Y. Self-assembled IR780-loaded transferrin nanoparticles as an imaging, targeting and PDT/PTT agent for cancer therapy. *Sci. Rep.* **2016**, *6*, 27421.

(44) Deepa, P. R.; Vandhana, S.; Jayanthi, U.; Krishnakumar, S. Therapeutic and toxicologic evaluation of anti-lipogenic agents in cancer cells compared with non-neoplastic cells. *Basic Clin. Pharmacol. Toxicol.* **2012**, *110*, 494–503.

(45) Manivasagan, P.; Oh, J. Production of a novel fucoidanase for the green synthesis of gold nanoparticles by *Streptomyces* sp. and its cytotoxic effect on HeLa cells. *Mar. Drugs* **2015**, *13*, 6818–6837.

(46) Pereira, M. I. A.; Monteiro, C. A. P.; de Oliveira, W. F.; Santos, B. S.; Fontes, A.; Cabral Filho, P. E., Resazurin-Based Assay to Evaluate Cell Viability After Quantum Dot Interaction. In *Quantum Dots*; Springer, 2020; pp 213–221.

(47) Chen, G.; Ågren, H.; Ohulchanskyy, T. Y.; Prasad, P. N. Light upconverting core–shell nanostructures: nanophotonic control for emerging applications. *Chem. Soc. Rev.* **2015**, *44*, 1680–1713.

(48) Gupta, A.; Ghosh, S.; Thakur, M. K.; Zhou, J.; Ostrikov, K. K.; Jin, D.; Chattopadhyay, S. Up-conversion hybrid nanomaterials for light and heat-driven applications. *Prog. Mater. Sci.* **2021**, *121*, No. 100838.

(49) Hagberg, G. E.; Scheffler, K. Effect of r1 and r2 relaxivity of gadolinium-based contrast agents on the T1-weighted MR signal at increasing magnetic field strengths. *Contrast Media Mol.* **2013**, *8*, 456–465.

(50) Sun, Y.; Zhu, X.; Peng, J.; Li, F. Core–shell lanthanide upconversion nanophosphors as four-modal probes for tumor angiogenesis imaging. *ACS Nano* **2013**, *7*, 11290–11300.

(51) Li, S.-D.; Huang, L. Pharmacokinetics and biodistribution of nanoparticles. *Mol. Pharmaceutics* **2008**, *5*, 496–504.

(52) Watcharin, W.; Schmithals, C.; Pleli, T.; Köberle, V.; Korkusuz, H.; Huebner, F.; Zeuzem, S.; Korf, H. W.; Vogl, T. J.; Rittmeyer, C. Biodegradable human serum albumin nanoparticles as contrast agents for the detection of hepatocellular carcinoma by magnetic resonance imaging. *Eur. J. Pharm. Biopharm.* **2014**, *87*, 132–141.

(53) Choi, H. S.; Liu, W.; Misra, P.; Tanaka, E.; Zimmer, J. P.; Ipe, B. I.; Bawendi, M. G.; Frangioni, J. V. Renal clearance of nanoparticles. *Nat. Biotechnol.* **2007**, *25*, 1165.

(54) Li, M.; Fang, H.; Liu, Q.; Gai, Y.; Yuan, L.; Wang, S.; Li, H.; Hou, Y.; Gao, M.; Lan, X. Red blood cell membrane-coated upconversion nanoparticles for pretargeted multimodality imaging of triple-negative breast cancer. *Biomater. Sci.* **2020**, *8*, 1802–1814.

(55) Han, G.-M.; Li, H.; Huang, X.-X.; Kong, D.-M. Simple synthesis of carboxyl-functionalized upconversion nanoparticles for biosensing and bioimaging applications. *Talanta* **2016**, *147*, 207–212.

(56) Zhang, J.; Tang, H.; Liu, Z.; Chen, B. Effects of major parameters of nanoparticles on their physical and chemical properties and recent application of nanodrug delivery system in targeted chemotherapy. *Int. J. Nanomed.* **2017**, *12*, 8483.

(57) Matsumura, Y.; Maeda, H. A new concept for macromolecular therapeutics in cancer chemotherapy: mechanism of tumoritropic accumulation of proteins and the antitumor agent smancs. *Cancer Res.* **1986**, *46*, 6387–6392.

(58) Fang, H.; Li, M.; Liu, Q.; Gai, Y.; Yuan, L.; Wang, S.; Zhang, X.; Ye, M.; Zhang, Y.; Gao, M. Ultra-sensitive nanoprobe modified with tumor cell membrane for UCL/MRI/PET multimodality precise imaging of triple-negative breast cancer. *Nanomicro Lett.* **2020**, *12*, 62.

(59) Daniels, T. R.; Bernabeu, E.; Rodríguez, J. A.; Patel, S.; Kozman, M.; Chiappetta, D. A.; Holler, E.; Ljubimova, J. Y.; Helguera, G.; Penichet, M. L. The transferrin receptor and the targeted delivery of therapeutic agents against cancer. *Biochim. Biophys. Acta* **2012**, *1820*, 291–317.

(60) Cresswell, G. M.; Wang, B.; Kischuk, E. M.; Broman, M. M.; Alfar, R. A.; Vickman, R. E.; Dimitrov, D. S.; Kularatne, S. A.; Sundaram, C. P.; Singhal, S. Folate Receptor Beta Designates Immunosuppressive Tumor-Associated Myeloid Cells That Can Be Reprogrammed with Folate-Targeted Drugs. *Cancer Res.* **2021**, *81*, 671–684.

(61) Low, P. S.; Henne, W. A.; Doorneweerd, D. D. Discovery and development of folic-acid-based receptor targeting for imaging and therapy of cancer and inflammatory diseases. *Acc. Chem. Res.* **2008**, *41*, 120–129.

(62) De Rosales, R. T. Potential clinical applications of bimodal PET-MRI or SPECT-MRI agents. *J. Labelled Compd. Radiopharm.* **2014**, *57*, 298–303.

(63) Zhang, X.; Ong'achwa Machuki, J.; Pan, W.; Cai, W.; Xi, Z.; Shen, F.; Zhang, L.; Yang, Y.; Gao, F.; Guan, M. Carbon nitride hollow theranostic nanoregulators executing laser-activatable water splitting for enhanced ultrasound/fluorescence imaging and cooperative phototherapy. *ACS Nano* **2020**, *14*, 4045–4060.

Recommended by ACS

Chelator-Free Conjugation of ^{99m}Tc and Gd^{3+} to PEGylated Nanographene Oxide for Dual-Modality SPECT/MR Imaging of Lymph Nodes

Tianye Cao, Mingwei Wang, *et al.*

NOVEMBER 17, 2017
ACS APPLIED MATERIALS & INTERFACES

READ 

A Dendrimer-Based Dual Radiodense Element-Containing Nanoplatforrm for Targeted Enhanced Tumor Computed Tomography Imaging

Tingting Xiao, Xiangyang Shi, *et al.*

MARCH 16, 2020
LANGMUIR

READ 

Radiolabeled RNA Nanoparticles for Highly Specific Targeting and Efficient Tumor Accumulation with Favorable In Vivo Biodistribution

Hongzhi Wang and Peixuan Guo

JULY 02, 2021
MOLECULAR PHARMACEUTICS

READ 

Preparation of Biopex-Supported Gold Nanoparticles as Potential Fiducial Markers for Image-Guided Radiation Therapy

Kai Ikeda, Tetsu Yonezawa, *et al.*

FEBRUARY 17, 2022
ACS APPLIED BIO MATERIALS

READ 

Get More Suggestions >